APPLIED PHYSICS

Interface reconstruction with emerging charge ordering in hexagonal manganite

Shaobo Cheng,[1,2]* Changsong Xu,[3,4]* Shiqing Deng,[1] Myung-Geun Han,[2] Shanyong Bao,[1] Jing Ma,[1] Cewen Nan,[1] Wenhui Duan,[4] Laurent Bellaiche,[3] Yimei Zhu,[2†] Jing Zhu[1†]

Multiferroic materials, which simultaneously have multiple orderings, hold promise for use in the next generation of memory devices. We report a novel self-assembled MnO double layer forming at the interface between a multiferroic $YMnO_3$ film and a *c*-Al_2O_3 substrate. The crystal structures and the valence states of this MnO double layer were studied by atomically resolved scanning transmission electron microscopy and spectroscopy, as well as density functional theory (DFT) calculations. A new type of charge ordering has been identified within this MnO layer, which also contributes to a polarization along the [001] direction. DFT calculations further establish the occurrence of multiple couplings between charge and lattice in this novel double layer, in addition to the polarization in nearby $YMnO_3$ single layer. The interface reconstruction reported here creates a new playground for emergent physics, such as giant ferroelectricity and strong magnetoelectric coupling, in manganite systems.

INTRODUCTION

Because numerous physical phenomena may take place at the interfaces, interface science is now an important branch of materials science that has attracted worldwide attention (*1*, *2*). Driven by the advancement of thin-film deposition techniques, new systems can be created, and the local chemistry, bonding, and electronic environment can be tailored accordingly. A fundamental topic for interface science is atomic and electronic reconstruction, that is, how the lattice, charge, spin, and orbit differ from the bulk at the interface. Materials with partially occupied d orbitals bring about opportunities for extraordinary electronic properties, for example, interfacial high-mobility two-dimensional (2D) electron gases and superconductivity (*3*, *4*). Recent studies on multiferroics also focused on artificial delicate interfaces, especially in some hexagonal systems. Typical examples include the room-temperature magnetoelectric coupling in the $LuFeO_3/LuFe_2O_4$ superlattice (*5*).

$YMnO_3$ is the prototype of hexagonal multiferroics, such as $RMnO_3$ and $RFeO_3$ (R: rare earth, Sc, and In), which have trimerization-mediated (*6*) magnetoelectric coupling between geometric ferroelectricity and frustrated antiferromagnetism (*7*, *8*). $YMnO_3$ has strongly correlated electrons that can possibly combine diverse functionalities (*6*). Its electron-electron and electron-lattice interactions may result in novel phenomena at the symmetry-breaking areas such as surfaces, interfaces, domain walls, and vortex cores (*9*–*15*). As a member of $YMnO_3$-type multiferroics, *h*-$LuFeO_3$ (having the $P6_3cm$ space group) has a crystal structure very similar with $YMnO_3$ (*16*), and in the bulk phase, its polymorph, $LuFe_2O_4$ [of the $R\bar{3}m$ space group], has been experimentally and theoretically proven to be stable (*17*). The latter compound, $LuFe_2O_4$, consists of FeO double layers, each of which contains two triangular Fe-O planes and is separated by Lu-O planes. $LuFe_2O_4$ is known for its charge ordering (CO)–induced ferroelectricity, with an Fe^{2+}/Fe^{3+} ratio of 2:1 in one sublayer and an Fe^{2+}/Fe^{3+} ratio of 1:2 in another sublayer (*5*, *18*). Its long-range ordering features, as well-defined states, have also been studied and analyzed from layered structures to 3D configurations (*19*, *20*). Because of the fact that both *h*-$LuFeO_3$ and $LuFe_2O_4$, as well as their superlattices, can be stabilized, one may thus wonder whether a MnO double layer can exist in the hexagonal manganite systems. A positive answer to this question may extend the range of multiferroic candidates and lead to novel magnetoelectric couplings.

Here, $YMnO_3$ films are grown on Al_2O_3 substrates by pulsed laser deposition (PLD) method, and some physical properties of these films can be found elsewhere (*10*). Delicate interfacial structures of $YMnO_3$ film/*c*-Al_2O_3 substrate were finely investigated at atomic scale with help of spherical aberration–corrected scanning transmission electron microscopy (C_s-corrected STEM) and electron energy-loss spectroscopy (EELS), as well as density functional theory (DFT) calculations. In contrast to the merely electronic reconstruction reported in perovskite systems (*21*, *22*), both electronic and structural reconstructions are found at the interface of $YMnO_3/Al_2O_3$ system. Specifically, a MnO double layer has been identified at the interface, and careful inspection reveals that the atomic structure of MnO double layer is very similar to FeO double layer in $LuFe_2O_4$, constructing a formula unit–thick syntactic layer of YMn_2O_4. A new type of CO within the reconstructed MnO double layer has been revealed by both EELS and DFT calculations. Our results establish the close correlation between charge and lattice, suggesting the tenability of functionalities by interfacial reconstruction in hexagonal multiferroic films.

RESULTS

The atomic models of polarized $YMnO_3$ and $LuFeO_3$ can be found in the Supplementary Materials. Three vicinal bipyramids trimerize and lead to the displacements of A-site ions (Y or Lu) along the *c* direction. Magnetic ions (Mn for $YMnO_3$ and Fe for $LuFeO_3$) form a 2D spin frustration system and contribute to (anti)ferromagnetism. A CO ferrite system $LuFe_2O_4$ is also illustrated. Ideally, except for the epitaxial relationship between an $YMnO_3$ film and an Al_2O_3 substrate, the in-plane direction satisfies $YMnO_3$ [100]//Al_2O_3 [100].

TEM experiments

Figure 1A shows the low-magnification bright-field transmission electron microscopy (TEM) image for the $YMnO_3$ thin film. The

[1]School of Materials Science and Engineering, Tsinghua University, Beijing 100084, China. [2]Department of Condensed Matter Physics and Materials Science, Brookhaven National Laboratory, Upton, NY 11973, USA. [3]Physics Department and Institute for Nanoscience and Engineering, University of Arkansas, Fayetteville, AR 72701, USA. [4]State Key Laboratory of Low-Dimensional Quantum Physics and Collaborative Innovation Center of Quantum Matter, Department of Physics, Tsinghua University, Beijing 100084, China.
*These authors contributed equally to this work.
†Corresponding author. Email: jzhu@mail.tsinghua.edu.cn (J.Z.); zhu@bnl.gov (Y.Z.)

interface between the $YMnO_3$ film and Al_2O_3 substrate is sharp and straight. The different contrast within the thin film is caused by in-plane rotation of the film, as discussed in the study of Cheng *et al.* (*10*). High-angle annular dark-field STEM (HAADF-STEM) images of $YMnO_3/Al_2O_3$ interface from [210] and [110] zone axes are shown in Fig. 1 (B and D, respectively). The Miller indexes are defined by the coordinate system of $YMnO_3$. The atomic contrast in HAADF image is only sensitive to heavy elements and correlated with the atomic number *Z*; that is, the heavier element has brighter atomic contrast (*23*). Interface between the $YMnO_3$ film and Al_2O_3 substrate can be distinguished because the atomic number of Al is much smaller than that of Y and Mn. In the $YMnO_3$ film, the ferroelectric displacement can be observed at the [110] zone axis. The quantitative result for the ferroelectric polarization values can be found in the Supplementary Materials (*11*). The ferroelectric value decreases at the interface but increases to bulk value very soon. The intensity profiles for atomic columns within the blue rectangle areas in Fig. 1 (B and D) can be found in Fig. 1 (C and E, respectively). Positions with higher intensities correspond to rows of Y ions, whereas the relative low intensities are for rows of Mn ions. Anomalously, according to two consecutive low intensities of the columns (framed in a red dashed rectangle), a MnO double layer emerges at the interfaces. The elemental energy-dispersive spectroscopy (EDS) mapping for the interfacial area can be found in the Supplementary Materials.

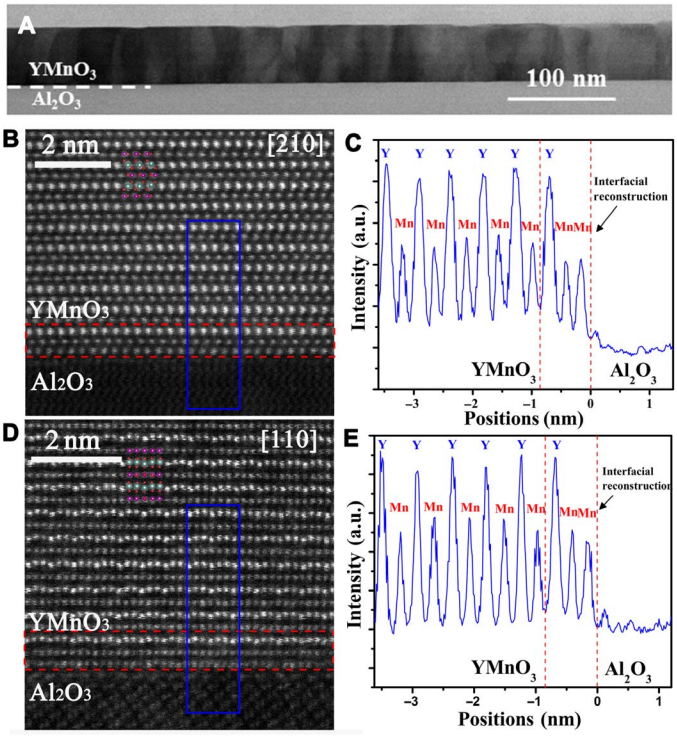

Fig. 1. (S)TEM images showing the interface between the $YMnO_3$ film and sapphire substrate. (**A**) Low-magnification bright-field TEM image for the $YMnO_3$ film. (**B**) HAADF image showing the interface between the $YMnO_3$ film and Al_2O_3 substrate from the [210] zone axis. The atomic model of $YMnO_3$ at the [210] zone axis is embedded. Y ions are in green, Mn ions are in purple, and O ions are in red. The reconstructed interfacial layer is highlighted in a red dashed rectangle. (**C**) Integrated intensity profile from top to bottom in the blue rectangle area in (B). The interfacial Y-Mn-Mn layer is shown between two red vertical lines. a.u., arbitrary units. (**D**) HAADF image for the interface taken at the [110] zone axis. (**E**) The corresponding integrated intensity profile from blue rectangle area in (D).

To reveal the accurate atomic structures at the interface, especially for the positions of oxygen, annular bright-field (ABF) images were acquired. In contrast to HAADF images, ABF images are sensitive to light elements (*24*). Considering the atomic structure of $YMnO_3$, the [210] zone axis is more suitable for observing oxygen. As shown in Fig. 2A, the atomic positions for oxygen in the $YMnO_3$ film, interfacial reconstructed layer, and Al_2O_3 substrate can all be identified. The oxygen bipyramids near the interface are distorted because of the large in-plane compressive strain provided by the Al_2O_3 substrate. The comparison of ABF images acquired from the interfacial area and the bulk area (area far from the interface) can be found in the Supplementary Materials. Careful inspections reveal that the atomic arrangement of reconstructed MnO double layers is analogous to the FeO double layer in $LuFe_2O_4$, forming a unit cell–thick syntactic layer of YMn_2O_4. As shown in Fig. 2B, it is difficult to identify oxygen from the [110] zone axis, because oxygen ions locate close to heavy elements along this direction. Atomic models near the interface are presented in both [210] and [110] zone axes as well. Combining the HAADF and ABF images from both [210] and [110] directions, one can determine that the Al_2O_3 substrate is terminated by a single Al^{3+} layer without any hints of surface reconstructions.

Considering the similar crystal structure of the reconstructed MnO double layer with the FeO double layer in $LuFe_2O_4$ [see, for example, the study of Mundy *et al.* (*5*)], CO could exist in this MnO double layer. The atomically resolved EELS spectra were acquired near the interfaces. The white arrow in Fig. 2A marks the EELS line-scan acquisition direction. The sequential numbers in Fig. 2C can be inferred in Fig. 2A. Extracted EELS results for Mn $L_{2,3}$ edges at different atomic layers can be found in Fig. 2C. The valence states of Mn ions (shown in Fig. 2D),

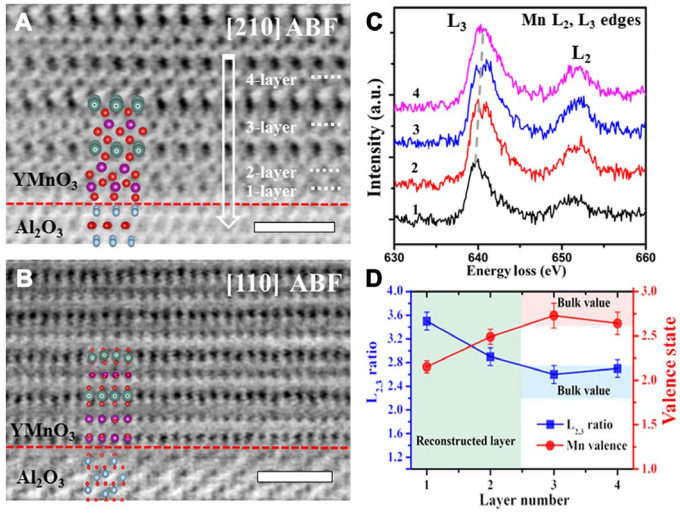

Fig. 2. ABF images and atomically resolved EELS results acquired from the interfacial areas. (**A**) ABF image showing the interface between the $YMnO_3$ film and Al_2O_3 substrate from the [210] zone axis. The white arrow shows the EELS line-scan direction. The sequential numbers for MnO layers are indicated. Scale bar, 1 nm. Atomic models for $YMnO_3$, interfacially reconstructed MnO double layer, and Al_2O_3 are embedded. The interface is marked by a horizontal red line. (**B**) ABF image acquired from the [110] zone axis. Atomic models from the [110] zone axis are overlaid, with Al, Y, Mn, and O atoms shown in blue, green, purple, and red, respectively. Scale bar, 1 nm. (**C**) Mn $L_{2,3}$ edges extracted from EELS line-scan results across the interface. The chemical shift can be indicated by the gray dashed line. (**D**) Evolution of $L_{2,3}$ ratios and the corresponding valence states of Mn ions.

calculated from the extracted $L_{2,3}$ area ratios (*25*), increase as deviating from the interface. The valence states of Mn ions at the interface have been measured for several times on different positions, and the error bars come from the statistic distributions. However, the valence-state distributions for two interfacial Mn layers show distinct characteristics from the scenario in $LuFe_2O_4$. Only one type of CO has been found in the MnO double layer according to our multiple measurements; that is, the Mn ions with lower valence states are always closer to the substrate. The Mn L_2 edges are aligned horizontally, and chemical shifts on Mn L_3 peaks caused by the variations of valence states are indicated by a gray dashed line in Fig. 2C.

DFT calculations

To explain our experimental results and provide more information, we also performed DFT calculations on a periodic superlattice $[(YMnO_3)/(YMn_2O_4)]_{\sqrt{3}\times\sqrt{3}\times2}$, with the "√3" being the length of the two in-plane lattice vectors in lattice constant units [leading to three Mn ions per (001) layer] and the "2" being the out-of-plane periodicity. This superlattice contains 72 atoms. It has two MnO double layers (each denoted as "Double layer" in Fig. 3A and consisting of a sublayer 1 and a sublayer 2 as indicated in Fig. 3B), two MnO single layers (each coined "Single layer" in Fig. 3A), and four single Y layers (two being termed "Y layer 1" and the other two being denoted as "Y layer 2"). It also satisfies the out-of-plane stacking rule that Y ions should be sandwiched along the *c* axis between two O ions belonging to the adjacent (001) MnO layers, as shown in Fig. 1 (B and D) and Fig. 4A. In the analysis of the DFT results, particular attention is paid to (i) the polarization occurring inside the $YMnO_3$ layers, (ii) structural features associated with the MnO double layers, and (iii) various possible COs that may exist in the MnO double layers. As we will demonstrate, items (i) to (iii) are strongly coupled together, implying coupled polarizations and a new type of charge-lattice interaction.

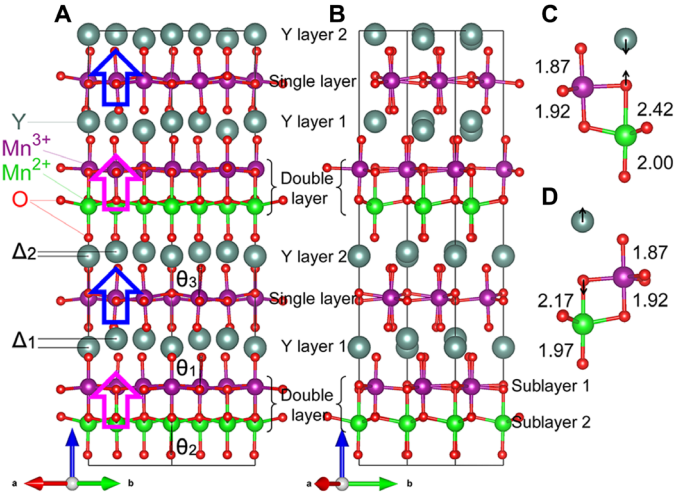

Fig. 3. Optimized ground state structure of $[(YMnO_3)/(YMn_2O_4)]_{\sqrt{3}\times\sqrt{3}\times2}$ superlattice, with a positive P_{sl} along with ST1 and CO3 arrangements (see text). (**A** and **B**) Atomic model viewing from the [110] and [210] directions, respectively. Δ_1 and Δ_2 indicate the relative displacements of Y ions along the *c*-axis direction, whereas θ_1, θ_2, and θ_3 represent the angles that MnO_5 tilt away from the *c* axis in different layers (see the Supplementary Materials). The hollow blue and pink arrows show the directions of the polarization in the MnO single layers and MnO double layers, respectively. (**C** and **D**) Atomic model of MnO double layers, with the Mn-O^{tp} bond lengths being indicated in black numbers (in Å). The black arrows indicate the relative displacements of Y and O ions in these two latter panels.

(i) Polarization of the $YMnO_3$ layers

Each of the $YMnO_3$ layers either has a ratio of 2:1 between Y ions moving up and down along the *c* axis or a ratio of 1:2 between these two types of Y ions. The first case corresponds to a polarization inside these $YMnO_3$ layers, P_{sl}, being up, that is, parallel to the *c* lattice vector. The second case is associated with a polarization pointing down, that is, being antiparallel to the *c* vector. Note that, as shown in Fig. 4 (B to G), only the first case is considered here, because P_{sl} pointing down can be deduced from a positive P_{sl} by simple symmetry. Note also that P_{sl} is known to be of improper origin, because it is induced by the K_3 zone–boundary phonon mode or the so-called "trimerization" (the Supplementary Materials provides details about trimerization in our superlattices) (*6*, *26*).

(ii) Structural features associated with the MnO double layers

It is numerically found that, for our superlattices, each MnO double layer can distort, with the resulting distortion rendering the Mn ions of the two sublayers being nonequivalent. One can then distinguish the two different structures by defining one as ST1 and another as ST2. The O ions that are in the same (001) layer with a selected Mn ion are defined as the equatorial O (O^{eq}) ions of that Mn ion, whereas the O ions that are on top of or below this Mn along the *c* axis are defined as its topical O (O^{tp}) ions. In these denotations, ST1 has shorter Mn-O^{tp} bonds in the sublayers 1 than in the sublayers 2, whereas the reversed hierarchy between these Mn-O^{tp} bonds in the sublayers 1 and 2 occurs for ST2, as shown in Fig. 4 (B and C, respectively). The notation O_i^{eq} and O_i^{tp} for equatorial and topical ions, for which $i = sl$, 1 and 2 correspond to the Mn ions being in the single layers, sublayers 1 and sublayers 2, respectively, as shown in Fig. 4A.

(iii) COs in the MnO double layers

Four types of COs (denoted as CO1, CO2, CO3, and CO4) are considered for the different Mn ions belonging to the MnO double layers. These Mn ions are differentiated by either initially setting their local magnetic moments to be 5 μ_B (which corresponds to the ideal case of Mn^{2+} ions) or 4 μ_B (which is associated with the ideal case of Mn^{3+} ions). The initial CO1 (CO2, respectively) arrangement has a ratio of one ideal Mn^{2+} ion versus two ideal Mn^{3+} ions in sublayers 1 (sublayers 2, respectively) and a ratio of two ideal Mn^{2+} ions versus one ideal Mn^{3+} ion in sublayers 2 (sublayers 1, respectively). On the other hand, the initial CO3 (CO4, respectively) configuration has only ideal Mn^{3+} ions in the sublayers 1 (sublayers 2, respectively) and only Mn^{2+} ions in the sublayers 2 (sublayers 1, respectively). Note also that these initial CO configurations are then allowed to relax both structurally (implying that some CO configurations can become unstable) and magnetically (leading to magnetic moments of the Mn ions having the possibility to deviate from the ideal values of 5 or 4 μ_B after convergence).

The relaxation of all presently studied configurations (resulting, for example, from the combination of two ST choices with four CO types) yields a predicted ground state that gathers CO3 arrangement, ST1 structure, and a positive P_{sl} polarization, as shown in Fig. 3 (A and B). Bader charges are further computed for this ground state (*27*), with the resulting valence states of Mn ions in sublayer 1, sublayer 2, and the Mn single layers being +1.60, +1.82, and +1.89, respectively. These values are much smaller than the ideal +2 and +3 charges that Mn ions can have, which is likely due to the ambiguity in dividing volume, but qualitatively agree with our experimental data in Fig. 2D. We will thus continue to denote the ions as Mn^{2+} and Mn^{3+} in the following text and figures. The charges of Mn can be computed in a different manner, which is by simply subtracting the relaxed magnetic moments of Mn ions from the value of 7 (the number of valence electrons in the

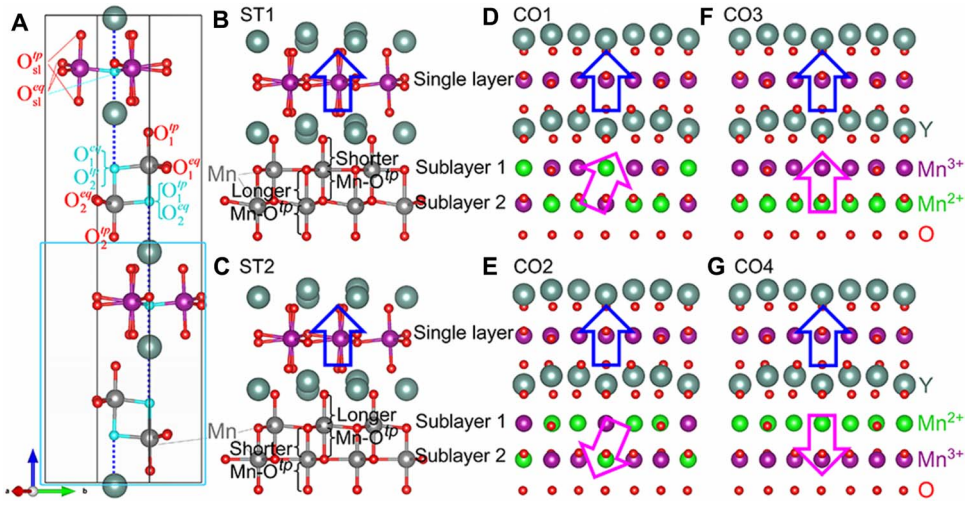

Fig. 4. Initial structures and charge order configurations used in our DFT calculations. (**A**) Schematics of the stacking rule. Y ions should be sandwiched along the *c* axis between two O ions belonging to adjacent (001) Mn-O layers. The vertical alignment of Y and these O ions are marked by dashed blue lines. The cyan rectangle marks half of the superlattice, which is then shown in the remaining panels of this figure. (**B** and **C**) ST1 and ST2 structures, respectively. (**D** to **G**) CO types ranging from CO1 to CO4, respectively, in the MnO double layers. Note that the polarization of the single $YMnO_3$ layer is set to be pointing up in all configurations, as indicated by the blue arrow. The direction of the polarization induced by CO in the MnO double layers is indicated by pink arrows. The green and purple spheres depict the nominal Mn^{2+} and Mn^{3+} ions, respectively.

presently used Mn pseudopotential). This subtraction gives valence states of +2.53, +3.03, and +3.09 for Mn ions in the sublayer 1, sublayer 2, and the Mn single layer (because the corresponding magnetic moments are 4.47, 3.97, and 3.91 μ_B, respectively), which also qualitatively agree with our corresponding experimental data and are fully consistent with the CO3 arrangement. One may thus conclude that only the relative values between charges of Mn ions is physical when comparing calculations with experiments, because the predicted absolute values depend on the method used to extract them.

Moreover, in the predicted ground state, the averaged Mn-O^{tp} bond length in sublayer 2 is 2.12 Å, whereas that in sublayer 1 is 1.90 Å (see Fig. 3, C and D). These numbers confirm that the determined ground state adopts a ST1 structure. Furthermore, it is found that the CO3 arrangement leads to a CO-induced polarization pointing along the *c* axis in the MnO double layer, which is the same direction than P_{sl} of the single $YMnO_3$ single layer. The ground state of the studied $YMnO_3$/YMn_2O_4 superlattice thus combines two different types of polarizations, the one of improper nature in $YMnO_3$ single-layer 1 and the one caused by CO in MnO double layers, in a head-to-tail way as shown in Fig. 4F. Note that this head-to-tail and CO3 arrangements are reported here for the first time in our combined experimental and computational work, because, for example, it was CO1 and CO2 that were observed in $LuFe_2O_4$ in the studies of Xiang and Whangbo (*28*) and Angst *et al.* (*29*) and in the FeO double layer of the $LuFeO_3$/$LuFe_2O_4$ superlattices (*5*).

The expected directions of the CO-induced polarization of the MnO double layers are also depicted in Fig. 4 (D, E, and G) for the CO1, CO2, and CO4 configurations (by means of magenta arrows), respectively, in the case of a ST1 structure and a positive P_{sl} (which is shown by blue arrows). These expected directions are deduced from what is known in $LuFe_2O_4$ (*6*). For instance, CO1 and CO2 have a polarization in the MnO double layers that is tilted away from the *c* axis, and combining a CO4 configuration with a positive P_{sl} results in head-to-head (or tail-to-tail) polarization patterns between the blue and magenta arrows. However, allowing the relaxation of the CO4 arrangement within ST1 and a positive P_{sl} leads to the transformation toward the predicted ground state, that is, CO3 (rather than CO4) arrangement along with ST1 and a positive P_{sl}. This fact emphasizes that the head-to-tail configuration is energetically preferred over the head-to-head (or tail-to-tail) patterns, which likely implies that applying and then removing an electric field along the *c* direction will lead to a transformation from a ground state having a CO3 arrangement and positive P_{sl} to another ground state but having a CO4 configuration with a negative P_{sl}. It is further numerically found that this transformation should also lead to a transition from ST1 to ST2. In other words, the calculations (but also symmetry analysis) show that the two combinations of (i) ST2 with CO4 and a negative P_{sl} and (ii) ST1 with CO3 and a positive P_{sl} yield the same energy, which demonstrates a cross coupling among P_{sl}, CO, and structures and establishes that a new type of charge-lattice effect exists in the $YMnO_3$/YMn_2O_4 systems. We have further checked the polarization dependence of the CO in MnO double layers. As shown in the Supplementary Materials, decreasing the polarization in $YMnO_3$ will not affect the CO in the MnO double layers.

The fact that the ground state combines ST1 and CO3 (or equivalently, ST2 and CO4) arrangements implies that Mn^{2+} ions always have longer Mn-O^{tp} bonds, whereas Mn^{3+} ions have shorter ones. To understand this fact, we analyze the 3d orbital occupation of MnO and also compare it with that of FeO double layers in $LuFe_2O_4$. Within the trigonal bipyramid crystal field, d orbitals of the Mn/Fe cation split into three energy levels: (i) the lowest doublet d_{xz} and d_{yz}, (ii) the doublet d_{xy} and $d_{x^2-y^2}$, and (iii) the highest singlet d_{z^2} (*30*). Figure 5 (A and B) indicates that Mn^{3+} and Mn^{2+} have $3d^4$ and $3d^5$ configurations, respectively, which lead to a vacant d_{z^2} orbital for Mn^{3+} and an occupied d_{z^2} orbital for Mn^{2+}. Further, Fig. 5 (C and D) shows that the hybridization between Mn/Fe d_{z^2} and O^{tp} p_z forms one bond state with lowered energy and one antibond state with higher energy. For $Mn^{3+}O_5$ with vacant d_{z^2} orbital, only the bond state is occupied, which thus results in short Mn-O^{tp} bond. On the other hand, for $Mn^{2+}O_5$ with occupied d_{z^2} orbital, both the bond and antibond states are occupied, which thus leads to long Mn-O^{tp} bonds. This effect results in the noncentrosymmetric

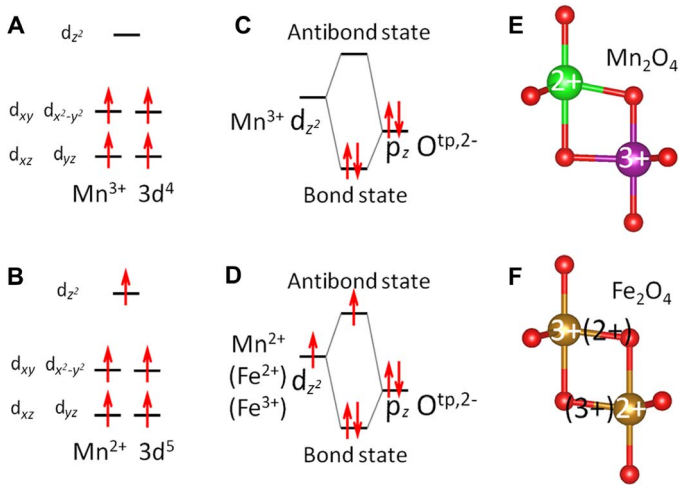

Fig. 5. Schematization of the 3d orbital occupancy and structural features of MnO versus FeO double layers. (**A** and **B**) 3d orbital occupancy for Mn^{3+} and Mn^{2+}, respectively. (**C**) Bond and antibond states between $O^{tp,2-}$ and Mn^{3+}. (**D**) Bond and antibond states involving the Mn^{2+}, Fe^{3+}, and Fe^{2+} ions, respectively. (**E** and **F**) Schematics of the noncentrosymmetric MnO and centrosymmetric FeO double layers, respectively. Small red spheres are O ions, whereas green, purple, and golden spheres are Mn^{2+}, Mn^{3+}, and Fe^{2+}/Fe^{3+}, respectively. Superscript numbers on Fe or Mn ions indicate the nominal valence states.

MnO double-layer structure shown in Fig. 5E. By contrast, $Fe^{3+}(3d^5)$ and $Fe^{2+}(3d^6)$ both have occupied d_{z^2} orbital, and thus, both occupied antibond state, which leads to centrosymmetric FeO double layer, as shown in Fig. 5F.

DISCUSSION

Note that, in our DFT calculations, decreasing the polarization of $YMnO_3$ layers does not affect the CO in MnO double layers. These facts, as well as the aforementioned special d orbital occupations in MnO double layers, strongly hint that the CO in YMn_2O_4 is much more robust than that in $LuFe_2O_4$. Considering that the CO transition temperature of $LuFe_2O_4$ is about 330 K, we thus expect the transition temperature of YMn_2O_4 to be even higher (and thus above room temperature) (*18*). Because bulk YMn_2O_4 bulk sample does not exist, we have limited knowledge about its physical properties at macroscopic scale. However, thin-film growth techniques can be applied for the growth of a $YMn_2O_4/YMnO_3$ superlattice in future. We note that the magnetic properties can be enhanced markedly in a $LuFe_2O_4/LuFeO_3$ superlattice system, whereas $LuFe_2O_4$ only has CO1 CO, which results in very small polarization. We expect that the realization of a $YMn_2O_4/YMnO_3$ system could not only improve its magnetic properties but also significantly increase its polarization, because the electric dipoles come from both the displacement of A-site Y ions and CO of B-site Mn ions. Physical properties of $YMn_2O_4/YMnO_3$ system can be thus tuned by charge, spin, and orbital degrees of freedom.

Moreover, the in-plane lattice parameters for $LuFe_2O_4$ are in between those of Al_2O_3 and $LuFeO_3$ (the in-plane matching relation is $Al_2O_3[100]//LuFe_2O_4[210]//LuFeO_3[100]$). The $LuFe_2O_4$-like phase (MnO double layer) is expected to have similar lattice parameters with $LuFe_2O_4$, because $YMnO_3$ and $LuFeO_3$ have close lattice constants. Consequently, the MnO double layer could act as a strain buffer layer to mediate the strain in the $YMnO_3/Al_2O_3$ system. Previously, we have reported that the in-plane compressive strain for the $YMnO_3$ film on the Al_2O_3 substrate is 13.56% (*10*), which is smaller than the lattice mismatch between $YMnO_3$ and Al_2O_3 (about 22.4%) (*8*). Unless the in-plane rotation mechanism detailed in the study of Cheng *et al.* (*10*) is occurring here, we expect the interfacial MnO double layer to also play a role in the strain relaxation of our whole system.

To sum up, in this work, by combining electron microscopy and ab initio calculations, we determined a novel reconstructed interfacial structure between Al_2O_3 and $YMnO_3$, as well as their CO. The distribution of valence states for the MnO double layer was studied both experimentally and theoretically. The ability to resolve the reconstructed heterojunctions enables us to reveal a new type of CO at atomic scale and discover novel properties with potential applications in a diverse range of scientific disciplines. Our results set a step forward for the exploration of emergent phenomena in manganite systems.

MATERIALS AND METHODS

Experimental design

The $YMnO_3/Al_2O_3$ films were grown by PLD method. Before deposition, the background vacuum of 7.5×10^{-4} mtorr was maintained. Growth conditions were optimized at 850°C for the temperature, 5 Hz for the laser pulse frequency, and 100 mtorr for the oxygen partial pressure. The film with the thickness of 30 nm was grown in 15 min, which implies that the growth rate can be estimated to be of 0.0293 unit cells per second. After growth, the film was in situ–annealed: It was first heated up to 900°C and kept for 10 min to fully relax the interface stress and then cooled down at the rate of 5°C/min.

The electron microscopy experiments in this work were carried out at room temperature both at the National Center for Electron Microscopy in Beijing with FEI Themis 60-300 TEM equipped with unique high brightness field emission gun and double correctors and at the Brookhaven National Laboratory with a JEOL ARM 200CF microscope with double correctors. For HAADF images, the convergent angle is 21.2 mrad, and the collection angle is 67 to 275 mrad. The collection semi-angle for ABF images is from 11 to 22.4 mrad. The dual energy-loss spectrometers attached to the TEMs were used for the acquisition of EELS spectra. All the core-loss EELS spectra shown in this work have already been corrected by the zero-loss peaks. The TEM samples were fabricated in a traditional way, including cutting, polishing, and ion milling. The thickness of the area used for ABF imaging was estimated to be 18 nm.

DFT parameters

DFT calculations were performed using Vienna ab initio simulation package (*31*). The generalized gradient approximation (GGA) and the Perdew-Burke-Ernzerhof functional for solids (*32*) were used here. A 400-eV plane wave cutoff energy was used for all calculations along with the projector-augmented wave method (*33*), with the Y (4s, 4p, 4d, and 5s), Mn (3d and 4s), and O (2s and 2p) electrons being treated as valence electrons. An effective Hubbard $U = 4$ eV was also used to treat the 3d electrons of Mn ions (*7*). Moreover, a $3 \times 3 \times 1$ k-point mesh was used for the considered supercells, and all Hellman-Feynman forces were imposed to be smaller than 0.01 eV/Å on each ion. Figures were prepared using the Visualization for Electronic and STructural Analysis (VESTA) software (*34*). Note also that the starting structure of MnO double layers is taken from the $R\bar{3}m$ phase of $LuFe_2O_4$ and that we did not include the Al_2O_3 substrate in the calculations due to the large lattice mismatch between $YMnO_3$ and this substrate.

SUPPLEMENTARY MATERIALS

Supplementary material for this article is available at http://advances.sciencemag.org/cgi/content/full/4/5/eaar4298/DC1

Supplementary Materials

fig. S1. Schematic atomic models.

fig. S2. Quantitative evaluation of polarization in the film.

fig. S3. EDS mapping results for the interface.

fig. S4. ABF images from the interfacial and the bulk areas.

fig. S5. Calculated $YMnO_3$ polarization dependence of CO in MnO double layers.

References (*35*, *36*)

REFERENCES AND NOTES

1. J. Mannhart, D. G. Schlom, Oxide interfaces—An opportunity for electronics. *Science* **327**, 1607–1611 (2010).
2. X. Li, M. Sun, C. Shan, Q. Chen, X. Wei, Mechanical properties of 2D materials studied by in situ microscopy techniques. *Adv. Mater. Interfaces* **5**, 1701246 (2018).
3. L. Yu, A. Zunger, A polarity-induced defect mechanism for conductivity and magnetism at polar-nonpolar oxide interfaces. *Nat. Commun.* **5**, 5118 (2014).
4. G. Koster, A. Brinkman, H. Hilgenkamp, A. J. H. M. Rijnders, D. H. A. Blank, High-T_c superconducting thin films with composition control on a sub-unit cell level; the effect of the polar nature of the cuprates. *J. Phys. Condens. Matter* **20**, 264007 (2008).
5. J. A. Mundy, C. M. Brooks, M. E. Holtz, J. A. Moyer, H. Das, A. F. Rébola, J. T. Heron, J. D. Clarkson, S. M. Disseler, Z. Liu, A. Farhan, R. Held, R. Hovden, E. Padgett, Q. Mao, H. Paik, R. Misra, L. F. Kourkoutis, E. Arenholz, A. Scholl, J. A. Borchers, W. D. Ratcliff, R. Ramesh, C. J. Fennie, P. Schiffer, D. A. Muller, D. G. Schlom, Atomically engineered ferroic layers yield a room-temperature magnetoelectric multiferroic. *Nature* **537**, 523–527 (2016).
6. B. B. Van Aken, T. T. M. Palstra, A. Filippetti, N. A. Spaldin, The origin of ferroelectricity in magnetoelectric $YMnO_3$. *Nat. Mater.* **3**, 164–170 (2004).
7. H. Tan, C. Xu, M. Li, S. Wang, B.-L. Gu, W. Duan, Pressure and strain effects of hexagonal rare-earth manganites: A first-principles study. *J. Phys. Condens. Matter* **28**, 126002 (2016).
8. C. Xu, Y. Yang, S. Wang, W. Duan, B. Gu, L. Bellaiche, Anomalous properties of hexagonal rare-earth ferrites from first principles. *Phys. Rev. B* **89**, 205122 (2014).
9. S. Cheng, J. Li, M.-G. Han, S. Deng, G. Tan, X. Zhang, J. Zhu, Y. Zhu, Topologically allowed nonsixfold vortices in a sixfold multiferroic material: Observation and classification. *Phys. Rev. Lett.* **118**, 145501 (2017).
10. S. Cheng, M. Li, S. Deng, S. Bao, P. Tang, W. Duan, J. Ma, C. Nan, J. Zhu, Manipulation of magnetic properties by oxygen vacancies in multiferroic $YMnO_3$. *Adv. Funct. Mater.* **26**, 3589–3598 (2016).
11. S. Cheng, M. Li, Q. Meng, W. Duan, Y. G. Zhao, X. F. Sun, Y. Zhu, J. Zhu, Electronic and crystal structure changes induced by in-plane oxygen vacancies in multiferroic $YMnO_3$. *Phys. Rev. B* **93**, 054409 (2016).
12. D. Meier, J. Seidel, A. Cano, K. Delaney, Y. Kumagai, M. Mostovoy, N. A. Spaldin, R. Ramesh, M. Fiebig, Anisotropic conductance at improper ferroelectric domain walls. *Nat. Mater.* **11**, 284–288 (2012).
13. S. Deng, S. Cheng, C. Xu, B. Ge, X. Sun, R. Yu, W. Duan, J. Zhu, Atomic mechanism of hybridization-dependent surface reconstruction with tailored functionality in hexagonal multiferroics. *ACS Appl. Mater. Interfaces* **9**, 27322–27331 (2017).
14. X. Wu, U. Petralanda, L. Zheng, Y. Ren, R. Hu, S.-W. Cheong, S. Artyukhin, K. Lai, Low-energy structural dynamics of ferroelectric domain walls in hexagonal rare-earth manganites. *Sci. Adv.* **3**, e1602371 (2017).
15. M. E. Holtz, K. Shapovalov, J. A. Mundy, C. S. Chang, Z. Yan, E. Bourret, D. A. Muller, D. Meier, A. Cano, Topological defects in hexagonal manganites: Inner structure and emergent electrostatics. *Nano Lett.* **17**, 5883–5890 (2017).
16. W. Wang, J. Zhao, W. Wang, Z. Gai, N. Balke, M. Chi, H. N. Lee, W. Tian, L. Zhu, X. Cheng, D. J. Keavney, J. Yi, T. Z. Ward, P. C. Snijders, H. M. Christen, W. Wu, J. Shen, X. Xu, Room-temperature multiferroic hexagonal $LuFeO_3$ films. *Phys. Rev. Lett.* **110**, 237601 (2013).
17. M. A. Subramanian, T. He, J. Chen, N. S. Rogado, T. G. Calvarese, A. W. Sleight, Giant room-temperature magnetodielectric response in the electronic ferroelectric $LuFe_2O_4$. *Adv. Mater.* **18**, 1737–1739 (2006).
18. N. Ikeda, H. Ohsumi, K. Ohwada, K. Ishii, T. Inami, K. Kakurai, Y. Murakami, K. Yoshii, S. Mori, Y. Horibe, H. Kitô, Ferroelectricity from iron valence ordering in the charge-frustrated system $LuFe_2O_4$. *Nature* **436**, 1136–1138 (2005).
19. Y. Zhang, H. X. Yang, C. Ma, H. F. Tian, J. Q. Li, Charge-stripe order in the electronic ferroelectric $LuFe_2O_4$. *Phys. Rev. Lett.* **98**, 247602 (2007).
20. Y. Zhang, H. X. Yang, Y. Q. Guo, C. Ma, H. F. Tian, J. L. Luo, J. Q. Li, Structure, charge ordering and physical properties of $LuFe_2O_4$. *Phys. Rev. B* **76**, 184105 (2007).
21. A. Ohtomo, H. Y. Hwang, A high-mobility electron gas at the $LaAlO_3/SrTiO_3$ heterointerface. *Nature* **427** 423–426 (2004).
22. A. Annadi, Q. Zhang, X. R. Wang, N. Tuzla, K. Gopinadhan, W. M. Lü, A. R. Barman, Z. Q. Liu, A. Srivastava, S. Saha, Y. L. Zhao, S. W. Zeng, S. Dhar, E. Olsson, B. Gu, S. Yunoki, S. Maekawa, H. Hilgenkamp, T. Venkatesan, Ariando, Anisotropic two-dimensional electron gas at the $LaAlO_3/SrTiO_3$ (110) interface. *Nat. Commun.* **4**, 1838 (2013).
23. L. Wu, F. Xu, Y. Zhu, A. B. Brady, J. Huang, J. L. Durham, E. Dooryhee, A. C. Marschilok, E. S. Takeuchi, K. J. Takeuchi, Structural defects of silver hollandite, $Ag_xMn_8O_y$, nanorods: Dramatic impact on electrochemisty. *ACS Nano* **9**, 8430–8439 (2015).
24. S. D. Findlay, N. Shibata, H. Sawada, E. Okunishi, Y. Kondo, T. Yamamoto, Y. Ikuhara, Robust atomic resolution imaging of light elements using scanning transmission electron microscopy. *Appl. Phys. Rev.* **95**, 191913 (2009).
25. H. K. Schmid, W. Mader, Oxidation states of Mn and Fe in various compound oxide systems. *Micron* **37**, 426–432 (2006).
26. C. J. Fennie, K. M. Rabe, Ferroelectric transition in $YMnO_3$ from first principles. *Phys. Rev. B* **72**, 100103(R) (2005).
27. G. Henkelman, A. Arnaldsson, H. Jónsson, A fast and robust algorithm for Bader decomposition of charge density. *Comput. Mater. Sci.* **36**, 354–360 (2006).
28. H. J. Xiang, M.-H. Whangbo, Charge order and the origin of giant magnetocapacitance in $LuFe_2O_4$. *Phys. Rev. Lett.* **98**, 246403 (2007).
29. M. Angst, R. P. Hermann, A. D. Christianson, M. D. Lumsden, C. Lee, M.-H. Whangbo, J.-W. Kim, P. J. Ryan, S. E. Nagler, W. Tian, R. Jin, B. C. Sales, D. Mandrus, Charge order in $LuFe_2O_4$: Antiferroelectric ground state and coupling to magnetism. *Phys. Rev. Lett.* **101**, 227601 (2008).
30. A. L. Companion, M. A. Komarynsky, Crystal field splitting diagrams. *J. Chem. Educ.* **41**, 257–262 (1964).
31. G. Kresse, D. Joubert, From ultrasoft pseudopotentials to the projector augmented-wave method. *Phys. Rev. B* **59**, 1758–1775 (1999).
32. J. P. Perdew, A. Ruzsinszky, G. I. Csonka, O. A. Vydrov, G. E. Scuseria, L. A. Constantin, X. Zhou, K. Burke, Restoring the density-gradient expansion for exchange in solids and surfaces. *Phys. Rev. Lett.* **100**, 136406 (2008).
33. P. E. Blöchl, Projector augmented-wave method. *Phys. Rev. B* **50**, 17953–17979 (1994).
34. K. Momma, F. Izumi, VESTA 3 for three-dimensional visualization of crystal, volumetric and morphology data. *J. Appl. Crystallogr.* **44**, 1272–1276 (2011).
35. H. Das, A. L. Wysocki, Y. Geng, W. Wu, C. J. Fennie, Bulk magnetoelectricity in the hexagonal manganites and ferrites. *Nat. Commun.* **5**, 2998 (2014).
36. D.-Y. Cho, J.-Y. Kim, B.-G. Park, K.-J. Rho, J.-H. Park, H.-J. Noh, B. J. Kim, S.-J. Oh, H.-M. Park, J.-S. Ahn, H. Ishibashi, S.-W. Cheong, J. H. Lee, P. Murugavel, T. W. Noh, A. Tanaka, T. Jo, Ferroelectricity driven by Y d^0-ness with rehybridization in $YMnO_3$. *Phys. Rev. Lett.* **98**, 217601 (2007).

Acknowledgments: We acknowledge the Arkansas High Performance Computing Center for the use of its supercomputers. **Funding:** This work was financially supported by the Chinese National Natural Science Foundation (11374174, 51390471, and 51527803), the National 973 Project of China (2015CB654902), and the National Key Research and Development Program (2016YFB0700402). This work made use of the resources of the National Center for Electron Microscopy in Beijing and the Brookhaven National Laboratory. Y.Z. would like to acknowledge the support by the U.S. Department of Energy (DOE) Basic Energy Sciences, Materials Sciences and Engineering Division under contract no. DE-SC0012704. C.X. and L.B. would like to acknowledge the financial support from the DOE, Office of Basic Energy Sciences, under Award # DE-SC0002220. **Author contributions:** S.C. and C.X. contributed equally to this work. S.C., S.D., and J.Z. conceived the project. The TEM experiments were conducted by S.C. under the guidance of J.Z. and Y.Z. The DFT calculations were carried out by C.X. under the supervision of W.D. and L.B. The thin-film samples were grown by S.B., J.M., and C.N. All authors discussed the results and commented on the manuscript. **Competing interests:** The authors declare that they have no competing interests. **Data and materials availability:** All data needed to evaluate the conclusions in the paper are present in the paper and/or the Supplementary Materials. Additional data related to this paper may be requested from the authors.

Submitted 7 November 2017
Accepted 5 April 2018
Published 18 May 2018
10.1126/sciadv.aar4298

Citation: S. Cheng, C. Xu, S. Deng, M.-G. Han, S. Bao, J. Ma, C. Nan, W. Duan, L. Bellaiche, Y. Zhu, J. Zhu, Interface reconstruction with emerging charge ordering in hexagonal manganite. *Sci. Adv.* **4**, eaar4298 (2018).